PCCP

ROYAL SOCIETY OF CHEMISTRY

PAPER

View Article Online
View Journal | View Issue

Check for updates

Cite this: *Phys. Chem. Chem. Phys.*, 2025, **27**, 24969

Stimuli-responsive gelation of Fmoc-L-tyrosine derivatives to form supramolecular architectures *via* cold atmospheric plasma treatment

Priya Bhatt, [ab] Pranadhika Das[a] and Kamatchi Sankaranarayanan *[ab]

The rapid self-assembly of peptides and amino acids into three-dimensional fibrous networks has been extensively investigated as a strategy for constructing supramolecular architectures. In this study, we demonstrate a unique strategy using cold atmospheric plasma (CAP) to assess the assembly behaviour of protected aromatic amino acid derivatives, such as Fmoc-L-tyrosine-OH and Fmoc-L-tyrosine(*t*Bu)-OH. CAP generates reactive species that induce hydrolysis and oxidation of amino acids, leading to the formation of the self-assembled fibrous micro-structured gels of Fmoc-tyrosine-OH and Fmoc-tyrosine(*t*Bu)-OH, underscoring the role of CAP-induced chemical transformations in modulating the hydrophobic–lipophilic balance of the assemblies. IR, CD and zeta potential analyses confirmed that the formation of these microstructures was primarily driven by aromatic interactions, π–π stacking, and other non-covalent interactions. Additionally, LC-MS analysis was employed to elucidate the molecular structural changes of the samples following CAP treatment, revealing the underlying mechanism of RONS-driven modifications. A remarkably low critical aggregation concentration (CAC) further demonstrates CAP's efficiency and reliability as a trigger for facilitating supramolecular assembly. The findings underscore CAP's versatility as a green, cost-effective, and tunable approach for the design of soft materials and the fabrication of peptide-based nanostructures, with significant potential in applications such as drug delivery, tissue engineering, and bioactive materials for diagnostics and therapeutic interventions.

Received 7th July 2025,
Accepted 23rd October 2025

DOI: 10.1039/d5cp02585k

rsc.li/pccp

Published on 29 ottobre 2025. Downloaded on 02/05/2026 06:27:29.

1. Introduction

Molecular self-assembly is a fundamental process in nature, playing a crucial role in the emergence and advancement of life.[1] One notable consequence of molecular self-assembly gives rise to supramolecular chemistry, which involves forming various types of supramolecular architectures. These architectures range from fibrils,[2,3] nanospheres,[4,5] nanorods,[6] and micelles[7,8] to complex 3D mesh-like structures,[9,10] giving rise to supramolecular hydrogels.[11,12] Unlike traditional polymeric hydrogels, which rely on covalently cross-linked polymer networks, supramolecular hydrogels form through noncovalent interactions such as π–π stacking, hydrogen bonding, and charge interactions. These supramolecular hydrogels have extensive applications in cell culture,[13,14] optoelectronics,[15] sensing,[16,17] and developing structured materials.

Fluoren-9-ylmethoxy carbonyl, commonly recognized as Fmoc, is a popular protecting group used in peptide synthesis. Fmoc facilitates hydrogenation and shows interesting aggregation properties as it contains bulky aromatic rings.[18] The aromatic–aromatic interactions play a pivotal role in stabilizing these self-assembled structures through non-covalent interactions such as π–π stacking, which enhance intermolecular hydrogen bonding.[19] This property has made Fmoc a popular N-terminal capping motif in peptide-based hydrogelators. Fmoc-protected amino acids and peptides are commercially available, cost-effective, and easily incorporated into self-assembling systems. The versatility of Fmoc-based hydrogelators continues to make them an attractive choice for designing functional biomaterials and has been studied extensively by several researchers over the last few years.[20–23] Transitioning from a non-gel state to a hydrogel requires a negative free energy change. Various stimuli can trigger this process, including pH changes, temperature shifts, solvent switching, redox reactions, and photochemical methods.[24] Here, we present a novel approach utilizing cold atmospheric plasma (CAP) to initiate the self-assembly of Fmoc-protected amino acids, potentially leading to the gelation of Fmoc-based conjugates and paving the way for new advancements in the field.

[a] *Physical Sciences Division, Institute of Advanced Study in Science and Technology, (An Autonomous Institute Under DST, Govt. of India), Vigyan Path, Paschim Boragaon, Garchuk, Guwahati, Assam 781035, India. E-mail: kamatchi.sankaran@gmail.com*

[b] *Academy of Scientific and Innovative Research (AcSIR), Campus Postal Staff College Area, Sector 19, Kamla Nehru Nagar, Ghaziabad 201002, Uttar Pradesh, India*

Published on 29 ottobre 2025. Downloaded on 02/05/2026 06:27:29.

Cold atmospheric plasma (CAP) is an emerging technology that has demonstrated versatility across various fields, including biomedicine,[25–27] materials science,[25,28,29] and environmental applications.[30,31] CAP generates a mixture of primary and secondary reactive species, such as ions, electrons, free radicals, reactive oxygen species (ROS), and reactive nitrogen species (RNS), which contribute to its broad functional capabilities.[32–35] These reactive species can induce surface modifications, facilitate chemical transformations, and trigger molecular self-assembly, making CAP a powerful tool for various applications. The ability of CAP to modulate intermolecular interactions and influence noncovalent bonding opens new possibilities in the field of supramolecular chemistry and biomaterial design. Unlike traditional methods of inducing self-assembly—such as pH shifts, solvent exchange, or thermal triggers—CAP provides a non-invasive, controllable, and efficient strategy to drive molecular organization. It does not produce any secondary pollutants and eliminates the need for additional chemicals to adjust pH or multiple solvents for processing, thus making it a greener and more affordable technology. Moreover, it is highly tunable and can be efficiently generated using atmospheric air at room temperature.

In this work, we have investigated the supramolecular properties of two L-tyrosine-derived Fmoc-modified amino acids using a helium-CAP jet. The motivation for selecting tyrosine-derived peptides came from our earlier understanding that the self-assembly of L-tyrosine can effectively be modulated, forming distinct nanoparticles using the CAP technique.[36] Therefore, we aimed to investigate the effects of protecting groups on L-tyrosine to shield its reactive sites and assess the resulting structural and functional changes post-CAP treatment. With this consideration, we selected two compounds for this article, Fmoc-L-tyrosine and Fmoc-L-tyrosine-*tert*-butyl, and studied their self-assembling properties in phosphate buffer. Several groups have studied the assembly properties of the Fmoc-tyrosine-derived peptides. Researchers have used the pH switch method,[37,38] solvent switch,[39,40] enzymatic reaction,[41] temperature control,[42] and irradiation to induce gelation in a phosphate buffer solution of Fmoc-tyrosine-OH.[37,38] Many have explored Fmoc-tyrosine as a functional biomaterial in drug delivery[43,44] and anti-bacterial[20] applications, among others. While there is enough research describing the gelation of Fmoc-tyrosine-OH, we found limited papers exploring the self-assembly or gelation of Fmoc-tyrosine(*t*Bu)-OH. In 2019, Aykent *et al.* discovered the gelation of L-tyrosine(*t*Bu)-OH in various solvents, including DMF, TFA, toluene, and butanol.[45] Conversely, CAP effectively eliminates the reliance on multiple chemicals traditionally required for gelation, making the process more cost-efficient and environmentally friendly. Beyond its role in directing self-assembly, CAP's inherent antimicrobial and antibacterial properties[46–48] offer an additional advantage in developing biomimetic materials, particularly by enhancing the stability and longevity of functional materials. The integration of CAP-driven self-assembly with its antimicrobial potential could lead to the creation of advanced bio-inspired materials with tailored properties, further expanding its impact in fields ranging from regenerative medicine to sustainable biomaterials.

2. Results and discussion

2.1 Fabrication of protected L-tyrosine self-assemblies using a cold atmospheric helium plasma jet

A base-labile amine-protecting group, 9-fluorenylmethoxycarbonyl (Fmoc), and an alcohol-protecting group, *tert*-butyl (*t*Bu), have been used in this experiment to check the self-assembly properties of the modified amino acids. Fmoc-L-tyrosine (Fmoc-Tyr-OH in this manuscript) and Fmoc-L-tyrosine(*t*Bu)-OH (Fmoc-Tyr(*t*Bu)-OH in this manuscript) were dissolved in 7.4 pH PBS at 1 mM. The self-assembly in the samples was induced by treating the sample solutions using a built-in CAP jet system (discussed in the Experimental section) for three different durations (t = 0, 5, and 10 min). As several reactive oxygen and nitrogen species (RONS) from the plasma plume interact with the solution phase of the sample, the plasma–liquid interaction gives rise to various other phenomena and generates several secondary species. These primary and secondary reactive species have the potential to alter the non-covalent interactions within the building blocks, thereby modifying or enhancing the self-assembly of the compounds. Interestingly, when Fmoc-Tyr(*t*Bu)-OH was irradiated under CAP, the molecules visibly assembled within approximately three minutes, forming a soft gel-like 3D structure in the bulk solution (Fig. 1(a)). Upon CAP exposure, we consistently observed the formation of gelatinous assemblies that appear to follow an enclosed, non-circular path (Fig. 1(a)) around the plasma plume. When the Petri dish was manually shifted, similar ring-like fibrous structures appeared at the new location exposed to the jet. To verify that the observed features were not artefacts of plume contact at a localised region, but rather the chemical/physical effects of plasma, we conducted an experiment where the sample was continuously stirred with a magnetic stirrer during CAP treatment. Fibrous, gelatinous structures still formed; however, the enclosed ring-like arrangements were disrupted by the bead's continuous agitation. This strongly suggests that gelation arises primarily from CAP-induced modulation of non-covalent interactions, such as hydrogen bonding, π–π stacking, or electrostatic interactions, which may trigger the self-assembly of Fmoc-modified amino acids into a 3D supramolecular assembly, discussed in detail in the later part of the manuscript.

In contrast to the above case, we found no visual observed gelation in the Fmoc-Tyr-OH samples after cold plasma treatment (Fig. 1(b)). To determine the concentration required for visual assembly formation in the samples, we tested it at various concentrations while keeping the CAP parameters constant. We made a stock solution of 25 mM and diluted it to six concentrations: 0.25 mM, 0.5 mM, 1 mM, 2 mM, 5 mM, and 10 mM. It was observed that Fmoc-Tyr(*t*Bu)-OH formed visible assemblies at concentrations above 0.5 mM, whereas no visible assemblies were detected at concentrations below 0.5 mM. In the case of Fmoc-Tyr-OH, the visual assemblies were seen at around 5 mM concentration (Fig. S3), suggesting that a similar visual assembly can be fabricated by Fmoc-Tyr-OH using CAP technology at an increased optimized concentration. Since the

 This journal is © the Owner Societies 2025

Published on 29 ottobre 2025. Downloaded on 02/05/2026 06:27:29.

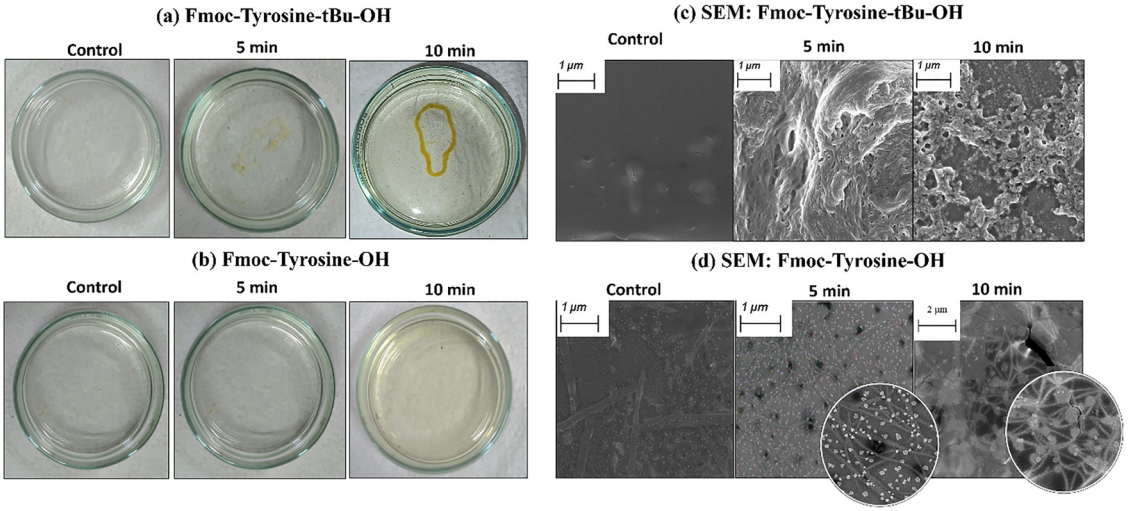

Fig. 1 CAP-treated samples of Fmoc-Tyr-OH and Fmoc-Tyr(*t*Bu)-OH (a) and (b) and SEM images of the samples (c) and (d).

work aims to check the effect of CAP treatment in the samples, we kept a uniform 1 mM concentration for all characterization. Various microscopic and biophysical techniques are employed to further investigate the formed assemblies.

For the Fmoc-Tyr(*t*Bu)-OH samples, the CAP-formed 3D supramolecular assemblies characterised under a SEM had a typical fibril structure with a porous morphology after 5- and 10-minute treatment (Fig. 1(c)). The fibrils have a diameter of 3–6 microns, as analysed by ImageJ. The Fmoc-Tyr-OH samples, however, showed the formation of some tubular, rod-like structures prior to treatment (Fig. 1(d)). After CAP treatment, these fibrils formed a more complex and entangled mesh-like structure.

AFM and TEM analyses were conducted to gain insights into the formed micro-architectures and further substantiate our findings. Interestingly, AFM and TEM imaging revealed that the untreated Fmoc-Tyr-OH sample also exhibited fibril-like structures, suggesting potential gelation behaviour in its native state (Fig. 2(a) and (c)). In addition to these fibrils, we also observed the formation of some particles in the CAP-10 min-treated samples (Fig. 2(b)), suggesting that such nanoparticulate domains co-existed within a fibril framework in Fmoc-Tyr samples. These particles were also

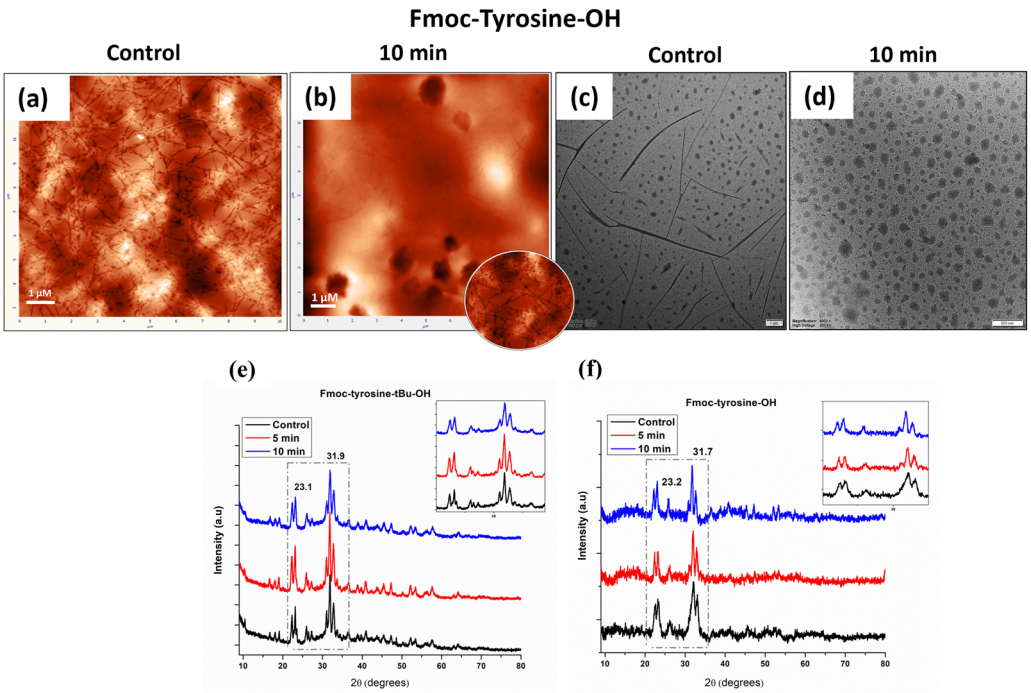

Fig. 2 AFM images (a, b) and TEM images (c, d) of Fmoc-Tyr-OH (top). XRD diffractograms (e, f) of untreated and CAP-treated Fmoc-Tyr(*t*Bu)-OH and Fmoc-Tyr-OH samples (bottom).

Published on 29 ottobre 2025. Downloaded on 02/05/2026 06:27:29.

observed in TEM analysis of the samples and had sizes on the order of a few nanometres (Fig. 2(c) and (d)). However, due to the extremely low concentration of samples deposited on the TEM copper grid, the electron microscopy may have preferentially emphasised the electron-dense nanodomains rather than the extended fibrillar structures. In one of our previous studies, such nanoparticle-like structures were also observed in L-tyrosine samples after helium-plasma jet treatment, having similar parameters.[36] The explanation was primarily attributed to the amine, carboxyl, and side chain functionalities of L-tyrosine, which were influenced by the synergistic effects of reactive species generated by CAP. It should be noted that all the above microscopic techniques use drying as a crucial step in method preparation; thus, they should be interpreted with consideration for the drying artefacts. A more advanced technique, such as cryo-TEM (or small-angle scattering), would provide a more accurate assessment of the native state of the assemblies and could be a future scope for the current work.

We performed powder XRD of the lyophilized samples to investigate the molecular arrangement of the samples after the CAP treatment. Fig. 2(e) and (f) shows the X-ray diffractogram of the untreated and CAP-treated samples. Peaks were seen around 32° and 23°, and both samples showed semi-crystalline behaviour. Furthermore, from crystallinity estimation (from integrated peak areas) and crystallite size evaluation (using the Scherrer equation), the crystallinity percentage was found to be around 77% in both samples, and it slightly decreased with an increase in the treatment time (Table 1). The decrease in the crystallinity of the samples is indicative of a more amorphous nature of the CAP-treated samples, as compared to the untreated samples. This behaviour is in accordance with our observation of CAP-induced gelation of the particles, since the gels have a characteristic of being amorphous in nature. This is because the long fibres form an amorphous matrix, entrapping the constituent molecules, thereby forming a localised ordered constraint and disrupted long-range order, a term sometimes referred to as "amorphous solidification".[49] This explains the reduction in the crystallinity of our CAP-induced supramolecular assemblies as compared to the crystalline untreated peptide solution. The average crystallite size in Fmoc-Tyr(*t*Bu) samples decreases after CAP-treatment, also validating the above discussion. In contrast, the increase in the crystallite size of Fmoc-Tyr samples from 17.07 nm to 22.7 nm in 10 min indicates that the amino acid solution has assembled into larger, more ordered nanodomains compared to their dispersed state in solution after plasma treatment. These nano-particles were also seen in the AFM and TEM images of CAP-treated Fmoc-Tyr samples.

Table 1 Crystallinity and crystallite size estimation of the CAP-treated samples

	Fmoc-Tyr(*t*Bu)-OH		Fmoc-Tyr-OH	
CAP treatment time	Average crystallite size (nm)	Crystallinity (%)	Average crystallite size (nm)	Crystallinity (%)
0 min	31.869	77.169	17.050	76.921
5 min	24.814	76.629	21.733	69.185
10 min	21.868	75.563	22.136	63.216

2.2 Mechanical and thermal stability of the formed self-assembled architectures

Using oscillatory rheology, the CAP-produced 3D supramolecular assemblies were characterized to understand their mechanical properties. Fig. 3(a) shows the evolution of the samples' storage modulus (G') and loss modulus (G'') with angular frequency. The formation of gels is characterized by $G' > G''$,[50] where G', G'', and the loss factor are independent for a typical strong gel. Although the loss factor showed an independence (Fig. S4), G'/G'' increased in the higher angular frequency regime. This dependency of storage and loss moduli on angular frequency is often a sign of the formation of weak gels or the possibility of sol-phase hydrogel formation.[51,52] The graphs (Fig. S5) highlight the point where the storage modulus begins to increase significantly, indicative of the sample's sol–gel transition point. It is observed that with the increase in the CAP-treatment time, the sol–gel transition point is shifting towards a lower value, suggesting that the CAP treatment leads to a decrease in the sol–gel transition point. This crossover frequency at which G' and G'' meet also indicates the physical crosslinking frequency, suggesting that the formed 3D-supramolecular assemblies might involve a reversible cross-linking phenomenon,[53] which can further be explored for their application as self-healing hydrogels.[12]

Furthermore, the viscosity of the samples was analysed as a function of the shear rate. A substantial decay of the sample's viscosity is observed over increasing shear, followed by a constant value at larger values. This curve illustrates how viscosity changes over time under an applied external shear, aiding in determining various rheological parameters.[54] Furthermore, at larger shear values, the viscosity of the CAP-treated solution is slightly higher. From the viscosity *vs.* shear rate curve (Fig. 3(b)) and shear stress *vs.* shear rate curve (Fig. 3(c)), it can be observed that initially, the flow type is near Newtonian as the stress *vs.* shear rate follows a linear trend; however, after CAP treatment, the type of flow follows a Bingham plastic flow,[55] resulting in a shear-thinning fluid. Hydrogels with such shear-thinning properties have massive potential as injectable biomaterials.[11]

We also investigated the rheology of the Fmoc-Tyr-OH samples before and after treatment to find a similar pattern in the storage and loss moduli (Fig. 3(d)–(f). This further confirms that the as-obtained Fmoc-Tyr-OH is a supramolecular gelatinous material, possessing the pourable characteristics of a viscoelastic fluid while maintaining the gel-like network structure,[56] as substantiated by the SEM, TEM, and AFM images. Additionally, no change in the viscosity was observed, and the nature of the flow remained the same post-CAP treatment.

Next, we checked the thermostability of the freeze-dried samples through differential scanning calorimetry (DSC). Thermal stability is a crucial parameter for characterizing supramolecular structures and refers to their structural rearrangement

 This journal is © the Owner Societies 2025

Published on 29 ottobre 2025. Downloaded on 02/05/2026 06:27:29.

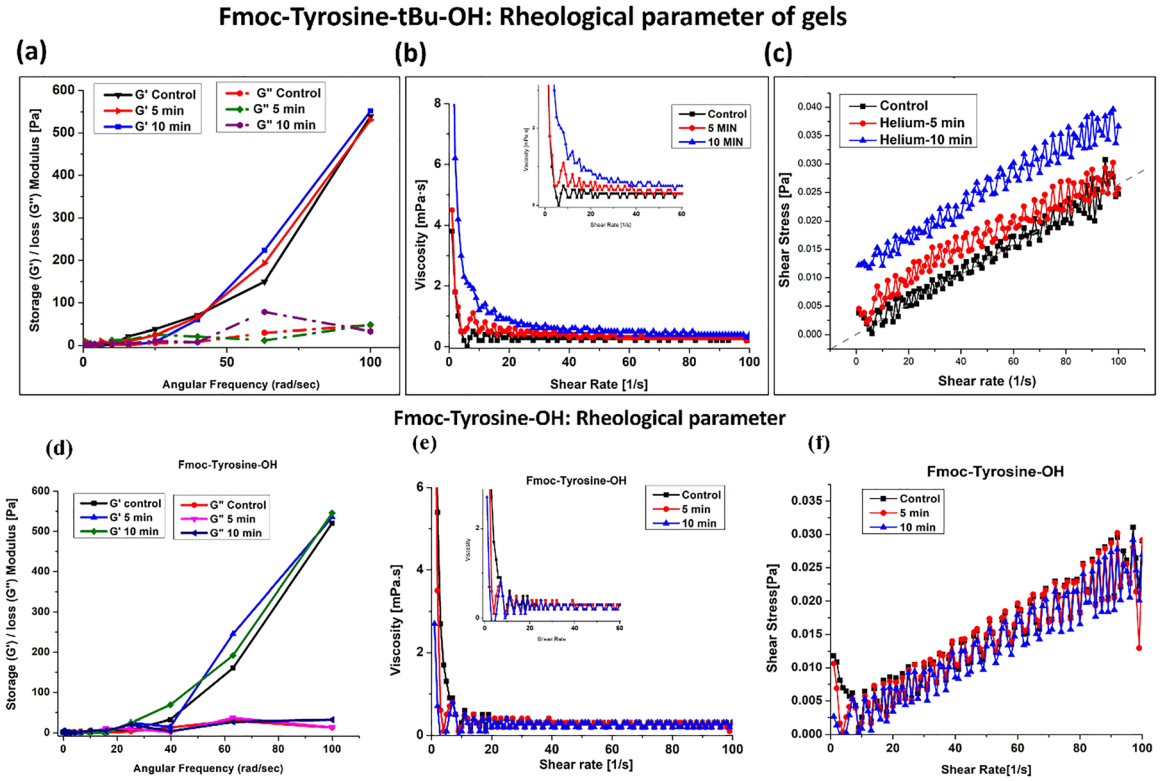

Fig. 3 Rheological analysis (a)–(c) of untreated and treated Fmoc-Tyr(*t*Bu) samples and (d)–(f) Fmoc-Tyr-OH samples.

at elevated temperatures. Evaluating this stability involves monitoring structural transitions as the temperature increases.[57] The transition point, represented as T_m, is a measure of structures' thermal stability, where a higher T_m value may indicate improved stability.[58] The DSC thermogram of the two compounds shows two peaks: the first peak at ~81 °C represents the transition point of the protein, while the second DSC peak, appearing at around 220 °C, might correspond to the complete degradation of the sample at such a high temperature [Fig. S6(a) and (b)]. Fig. 4(a) and (b) shows the expanded thermogram of the DSC peaks at ~81–86 °C, which shows a shift in the T_m towards a higher value (around 4-°C shift) after CAP-10-minute treatment in the case of Fmoc-Tyr(*t*Bu)-OH, which can suggest the relatively higher thermal stability of the CAP-treated samples compared to Fmoc-Tyr-OH samples with a less significant T_m change. Another parameter used in measuring thermal stability is the change in the enthalpy of unfolding (ΔH). It is calculated as the area under the DSC thermogram. A larger area points towards a higher enthalpy; thus, more energy is required to denature the protein. Fig. 4(a) and (b) also shows that the area under the curve increases after the treatment of the samples, suggesting a higher enthalpy. The numerical value of

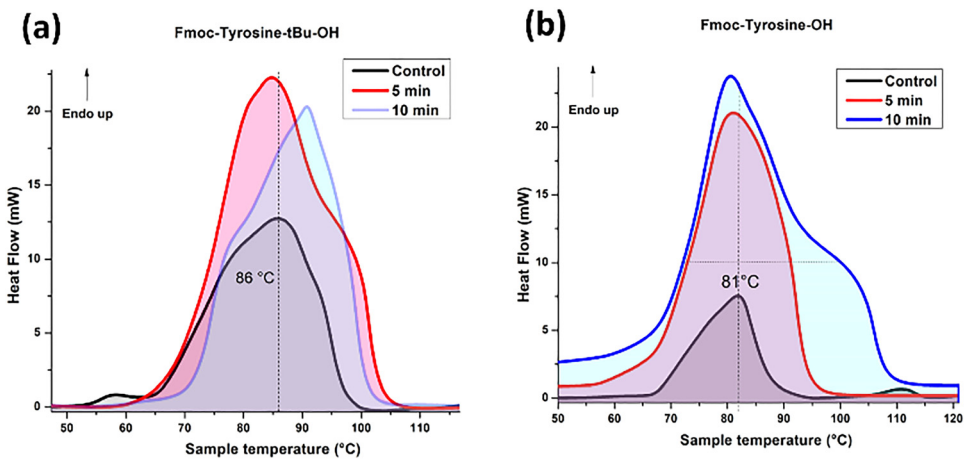

Fig. 4 DSC thermograms of (a) Fmoc-Tyr(*t*Bu)-OH and (b) Fmoc-Tyr-OH samples at the transition point.

Published on 29 ottobre 2025. Downloaded on 02/05/2026 06:27:29.

the area calculated is listed in Table S1 of the SI. A shift towards a greater enthalpy change indicates a stronger transition, which results from forming more stable structures, probably due to the formation of a higher-ordered structure post-CAP treatment.

2.3 Spectroscopic analysis of the CAP-treated samples

We further inquired about the differences in the atomic excitation levels for the two groups and the role of protection groups in the CAP-induced supramolecular assemblies of the samples for a better understanding of the mechanism. The Fmoc-protecting group typically shows two electronic bands at different wavelength ranges under UV-visible irradiation. The first K band is seen in the range of 200–220 nm due to the π–π* transition in the conjugated system, while the B band is observed in the 250–300 nm range due to the chromophores present in the aromatic moieties.[39] The UV-vis spectra of the Fmoc-protected molecules in the wavelength range of 250–300 nm showed three distinct peaks: an intense band at 265 nm and two moderately intense bands at 290 nm and 300 nm (Fig. 3(a) and (b)). The three peaks of the Fmoc-protected aromatic amino acid group arise due to the three groups of bands of the Fmoc-modified aromatic group.[59] This is why the other Fmoc-protected amino acid groups show similar absorbance spectra.[52,59] Fmoc has similar spectra to fluorene with peaks at 265 nm, 290 nm, and 300 nm, which are considered to be ascribed to the B_2 symmetry electronic transitions of the fluorene.[59,60] Thus, the K band, due to the side chain of L-tyrosine, observed at 220 nm, is overlapped by the Fmoc group's K band. As a result of the CAP-treatment, a hypochromic shift is observed with a slight blue shift of the peaks, explaining the possible aggregation phenomenon in the samples post-CAP treatment. Firstly, the blue shifting ($\Delta\lambda \approx 2$ nm) of the 220 nm peak is observed for the Fmoc-Tyr(*t*Bu) samples (Fig. S7(a) and (b)). A shift towards a shorter wavelength of the K-band in Fmoc often corresponds to the H-aggregation, a type of π–π stacking pattern where molecules stack in a face-to-face arrangement.[61,62] Both H- and J-aggregation result in the shifting of the peak (blue and red shifts, respectively). However, no shifting of the peaks is observed for the Fmoc-Tyr samples, indicating that self-assembled structures formed in the Fmoc-Tyr may be due to a combined effect arising from other interactions. This was further substantiated by the decrease in the absorbance intensity of Fmoc-Tyr-OH, which is much more trivial than the Fmoc-Tyr(*t*Bu)-OH group (Fig. 5(a) and (b)). The additional *t*Bu-group protects the side chain from interacting with the CAP-induced radicals in the solvent, probably resulting in a different aggregation phenomenon. The interactions from CAP radicals can affect the chromophores' electronic transitions and energy levels, giving rise to several aggregation phenomena. The decrease in the absorbance intensity might also result from reducing the turbidity of the Fmoc-Tyr(*t*Bu)-OH samples as aggregation begins, reinforcing the explanation for the aggregation differences between the two groups and prompting a deeper investigation into the spectroscopic intricacies.[63,64]

We further investigated the fluorescence spectra of the two groups. The aromatic side chain of the aromatic amino acid has an intrinsic fluorescence, which shows a maximum emission peak at the wavelength of 311–312 nm for both compounds at $\lambda_{max} = 265$ nm. This peak differs from the native tyrosine peak,[65]

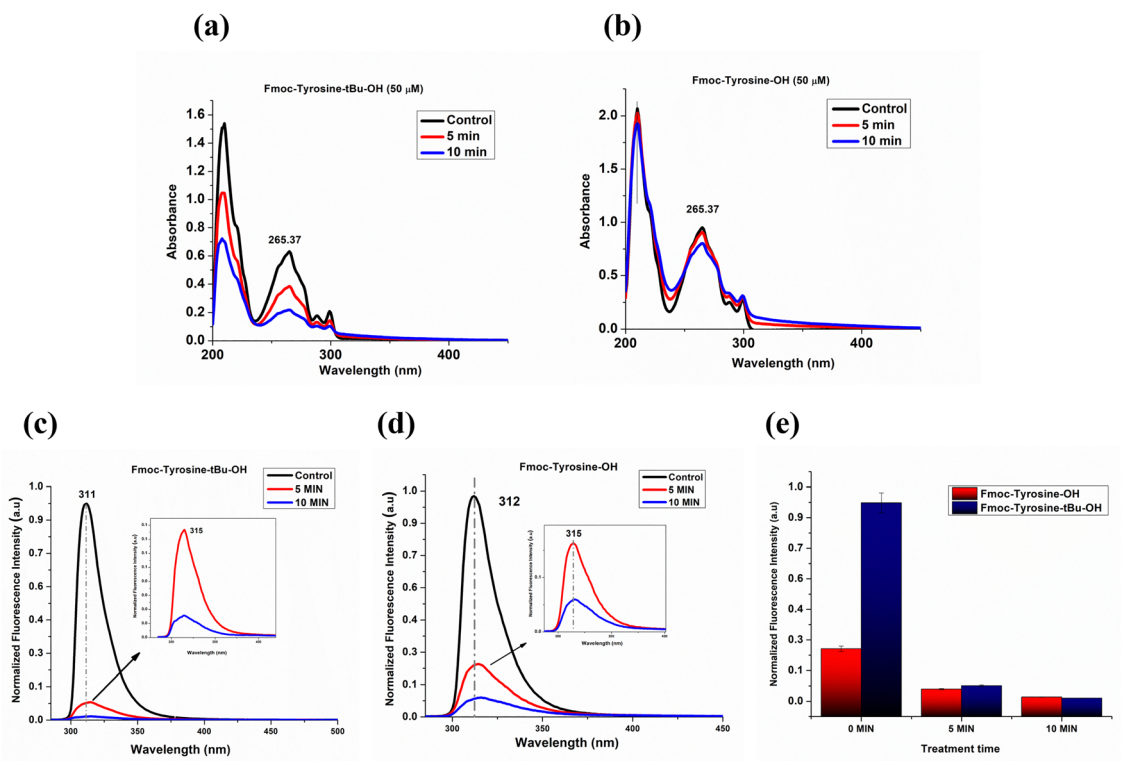

Fig. 5 UV-Visible (a) and (b) and fluorescence intensities (c) and (d) and comparison of the intensities (e).

 This journal is © the Owner Societies 2025

Published on 29 ottobre 2025. Downloaded on 02/05/2026 06:27:29.

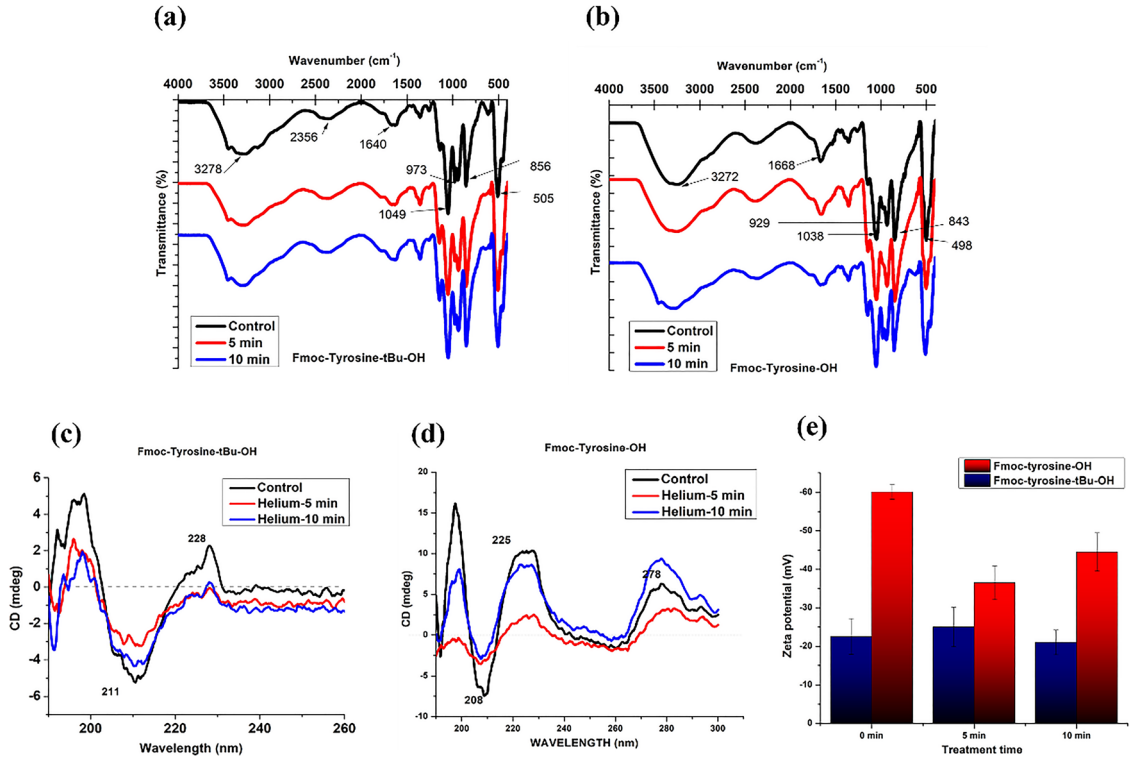

Fig. 6 FTIR analysis (a) and (b), CD spectroscopy (c) and (d), and zeta potential analysis (e) of Fmoc-Tyr(*t*Bu)-OH and Fmoc-Tyr-OH.

which shows emission around 304–305 nm attributed to the altered electronic environment introduced by the protecting groups on the amino acid. As seen in Fig. 5(c) and (d), there is a substantial decrease in the fluorescence intensity of both compounds. This decrease in intensity corresponds to the aggregation-caused quenching (ACQ) resulting from the π–π stacking of aromatic side chains and the Fmoc-group.[39] In addition to the quenching, both samples have a bathochromic shift with a wavelength change of around $\Delta\lambda = 4 \pm 1$ nm (shown in the inset). This shift towards a lower wavelength generally confirms the π–π stacking in the samples, as π–π interactions lower the energy of the emitted fluorescence.[39,66] However, here also, we can observe a much more intense quenching phenomenon of Fmoc-tyrosine(*t*Bu)-OH, compared to Fmoc-Tyr-OH (Fig. 4(e)). We suggest that the CAP-reactive species increases the propensity of the π–π interactions in both samples, indicated by a similar shift in the wavelength peaks. At the same time, it induces more aggregation in the Fmoc-Tyr(*t*Bu)-OH group, specified by a more substantial quenching resulting in the ACQ. Although the reactive species from the CAP is known to drive protein self-assembly by reacting with amino acids,[52,67] its interaction with the Fmoc-group increases the overall aromaticity of the compound, thus enhancing the gelation capability of the chosen compounds. The *tert*-butyl group further increases the overall bulk of the molecule and causes pronounced steric hindrance. This is likely to increase the hydrophobicity of the samples, resulting in a more intense quenching phenomenon and producing visible nanostructured gels post-CAP treatment.

To understand the changes in the secondary structures of the given peptides post-CAP treatment, IR spectroscopy of the freeze-dried samples was carried out. Fig. 6(a) and (b) shows the registered frequencies in the IR spectra. Post-CAP treatment, a few changes were observed in both the compounds' IR spectra. In both samples, the intensity of the peaks at 930–972 cm^{-1} was observed to be modulated post-treatment. This peak corresponds to the C=C bonds of the aromatic ring,[52] providing information on hydrogen bonding. In addition to that, peaks around 1600–1700 cm^{-1} are observed in both samples, usually considered to arise due to the carbamate group present in Fmoc samples. However, a single broad peak at 1650 cm^{-1} also corresponds to the random coil orientations in proteins, which is assigned to the disordered or imperfect amide stacking.[68] However, the FTIR spectra of CAP-treated samples exhibit no significant changes in either protected group, as evidenced by the absence of peak shifts, appearances, or disappearances. Further investigations are required to confirm any changes in the chemical alterations in the molecular structures.

CD spectroscopy was performed to check the changes in the chirality of the formed supramolecular assemblies in the samples. Both the samples were chiral active in the native form with peaks at 211 nm and 228 nm for the Fmoc-tyrosine(*t*Bu)-OH group and at 208 nm, 225 nm, and 278 nm for the Fmoc-Tyr-OH samples (Fig. 6(c) and (d)). The CD peaks at around 210–220 nm are due to the n–π* transition and those at 240–260 nm are due to the π–π* transition. The negative minimum at 208–211 nm is attributed to the β-sheet structure of the molecular assembly.[69] Earlier research has shown that CD

Published on 29 ottobre 2025. Downloaded on 02/05/2026 06:27:29.

peaks around 250–300 nm in a solution phase of Fmoc-tyrosine arise due to the chirality of the tyrosine component,[41] which is seen as a positive peak at 278 nm. However, we did not find this peak for the Fmoc-tyrosine(*t*Bu)-OH samples, probably because of the additional *t*Bu group shielding. Besides, we did not find any change in the orientation of the chirality in the CAP-treated samples in either of the groups, indicating no change in the folding of the proteins after CAP treatment. One limitation of CD is the necessity of diluting the samples to an optimised concentration, which compelled us to dilute them to an optimum concentration to get the noise-free signals, which might have affected the results.

Zeta potential analysis was performed to determine the electrostatic charges of the particles. Fig. 6(e) shows the variation in the zeta potential values of the two groups. All samples exhibited a negative charge, with Fmoc-Tyr-OH samples possessing a more negative charge than the Fmoc-tyrosine(*t*Bu)-OH group, with the latter showing almost half the value. This might be expected because the Fmoc-tyrosine's highly negative charge is neutralised by adding the *tert*-butyl group in the phenolic side chain of tyrosine, potentially preventing deprotonation. When CAP radicals interact with the two groups, a notable change in the zeta potential is observed for Fmoc-tyrosine, whereas Fmoc-tyrosine(*t*Bu) samples show minimal variation. This indicates that a protecting group in the side chain of tyrosine hinders the electrostatic interactions due to the CAP radicals. This could suggest that protonation of the side chain of tyrosine is not responsible for the observed gelation as it is entirely shielded by the *t*Bu group, further emphasizing the interaction of CAP-induced reactive species with the tyrosine chain.

CAP is widely recognized for generating a broad spectrum of reactive species through its direct interaction with its components and the formation of secondary and tertiary reactive species in the solvent system. These reactive species play a crucial role in inducing oxidation, hydroxylation, nitration, and other modifications when interacting with amino acid side chains,[36,70,71] in addition to influencing the zeta potential of amino acids. The resulting electrostatic interactions, charge transfer, and polarization effects typically lead to alterations in hydrogen bond formation, further impacting self-assembly dynamics.[72]

We further examined the changes in the structures of the compound due to the potential interactions and modifications induced by ROS/RNS exposure, including oxidation, hydroxylation, nitration, and other chemical alterations. LC-tandem mass spectrometry was employed to investigate the fragmentation pattern of the untreated and CAP-treated samples. The numerous peaks in the chromatogram result from a combination of fragmentation, adduct formation, impurities, multiple charge states, and solvent effects. For simplicity, we first focused on the most intense peaks in the chromatogram and compared the untreated chromatograms with those of the treated ones. The exact mass and elemental composition of the parent compound of Fmoc-tyrosine are 403.46 and $C_{24}H_{21}NO_5$, respectively. Although a peak at 403.21 is seen in all the chromatograms, the most abundant peak is observed at an *m*/*z* value of 402.21, corresponding to the deprotonated Fmoc-Tyr-OH samples$[M–H]^-$, mainly due to the negative scan mass spectra, in Fig. 7(a). The next intense peak in the chromatogram is at an *m*/*z* value of 446.24, which corresponds to an additional mass of 44.03. This peak for the native compound may arise due to the interaction of Fmoc-Tyr-OH with the solvent or mobile phase, possibly resulting in the carboxylation of the parent compound ($HCOO^-$). Moreover, this peak is also observed for all the other treated samples. Thus, it does not have significance in our current finding of CAP-induced modifications and is thus ignored.

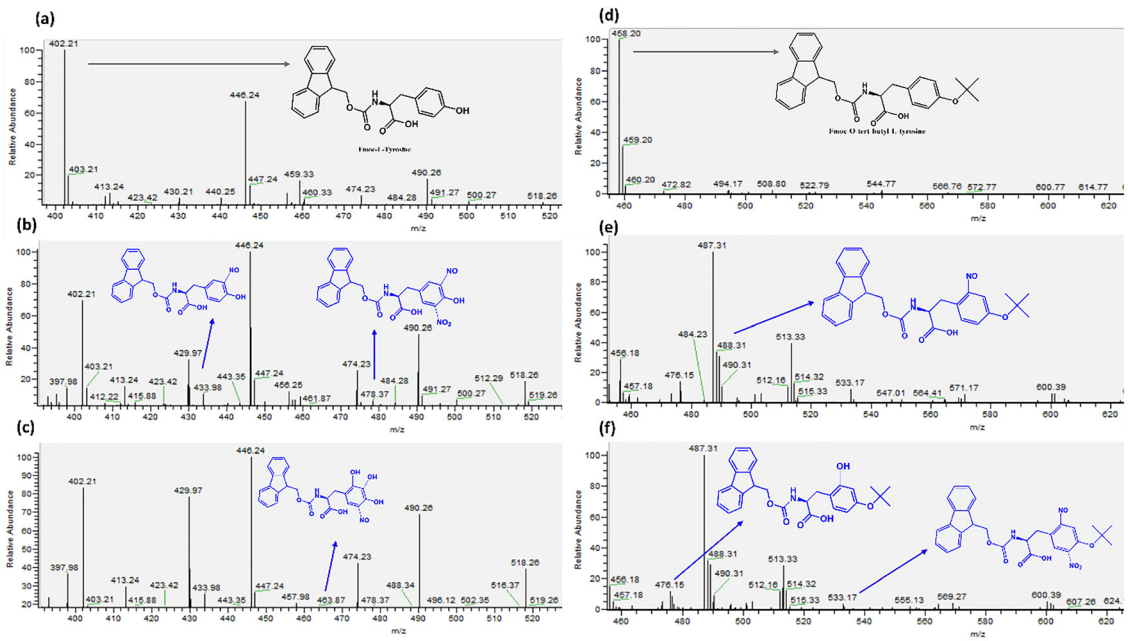

Fig. 7 LC-mass spectroscopy of untreated and CAP-treated samples of Fmoc-Tyr-OH (a)–(c) and Fmoc-Tyr(*t*Bu)-OH group (d)–(f).

 This journal is © the Owner Societies 2025

Published on 29 ottobre 2025. Downloaded on 02/05/2026 06:27:29.

The first distinct peak for both 5-minute and 10-minute CAP-treated samples is observed at *m*/*z* values of 429.97 and 433.98 (Fig. 7(b) and (c)). Nitrosation (addition of nitric oxide) of tyrosine's phenol group, with a slight rearrangement or protonation, is a strong possibility for the observed *m*/*z* 27.77 and 31.78 shifts, respectively. Such nitrosation is a possible reaction in many tyrosine oxidation/nitration pathways in the presence of oxidants and radicals.[73,74] Another peak at 461.87 and 463.87 observed in the 5-minute and 10-minute samples might arise due to the possible effect of hydroxylation and nitration of the aromatic moiety. The possible chemical structures of the observed peaks are drawn in Fig. 7.

In addition to the emergence of the above-mentioned new peaks in the CAP-treated samples, we can observe variations in the intensity of many peaks following CAP treatment. The CAP-treated samples showed a shift in the native peak at 402.21 and 403.21 to the *m*/*z* values 429.97, 474.23, 490.26, and 518.26, suggesting the post-treatment chemical modifications of the native compound. Additionally, peaks with lower *m*/*z* values were observed at 397.98. The slight shift in protonation states or rearrangement of functional groups under plasma conditions could lead to this mass decrease.

Likewise, the exact mass of Fmoc-tyrosine(*t*Bu)-OH is 459.53, with the elemental composition of $C_{28}H_{29}NO_5$. The observed *m*/*z* value of 458.21 likely corresponds to a molecule's $[M–H]^-$ deprotonated ion with an exact mass of 459.53 in negative mode (Fig. 7(d)). A distinct peak was observed at the *m*/*z* value of 476.15, resulting in a mass difference of 16.63, which is likely due to the hydroxylation of the molecule, possibly involving the aromatic ring of the amino acid. Another new peak for the CAP-treated samples is observed at *m*/*z* 488.31, resulting in a mass shift of 28.78, which may be attributed to the nitrosation (NO = +30 shift) of the compound. Another peak observed at 513.33 suggests a 55.1 Da shift from the parent mass (Fig. 7e and f). This peak may have arisen due to nitration (NO_2 = +46 shift) and nitrosation (NO = +30 shift) in the aromatic moieties of the compound, along with the removal of a water molecule and deprotonation of the sample. All the other peaks around it, *i.e.*, 512.16, 514.33, and 515.33, result from molecule rearrangement *via* protonation and deprotonation of the compound.

In both the treated samples, we observed similar peaks with slight variations in the intensity. In addition, peaks with lower *m*/*z* values were observed at 456.18 and 457.18, likely due to the minor deprotonation effects resulting from exposure to reactive species after treatment. It is worth noting that the current analysis was conducted based on the differences in *m*/*z* values obtained after fragmentation using a tandem mass spectrometer (MS/MS). While these assignments are done using a high-resolution accurate mass (HRAM) spectrometer, confirmation with authentic standards is required for further support of the data.

The LC-MS analysis revealed the addition of nitro and hydroxyl groups to the phenolic ring of the compounds, suggesting that these CAP-induced chemical modifications play an important role in triggering the observed assemblies. Such modifications are likely to alter the overall balance of non-covalent interactions in the solvent, thereby promoting the self-assembly process. A detailed discussion of these post-treatment chemical changes and their mechanistic implications is provided later in the text.

In our previous work, using the same parameters for plasma production, we quantified the reactive species generated by the helium plasma jet over 5- and 10-minute exposure with various chemical probes.[36,75,76] In addition, we subjected our samples to treatment with two distinct reactive species to assess their individual effects. Hydrogen peroxide (H_2O_2) and nitrate (NO_3^-) were introduced into the control samples at concentrations equivalent to those generated by CAP. However, neither reactive species independently induced any visible gelation (Fig. S8). The PL showed minimal quenching with the addition of 0.002% H_2O_2 ($\sim$587 μM) and 10 μM NO_3^- (Fig. S9). This analysis underscores that the aggregation behaviour observed in CAP-treated Fmoc-modified tyrosine derivatives results from the synergistic interaction between cold atmospheric plasma and various moieties present in the compound, including the amino acid side chain, carboxyl group, and protecting groups, all of which contribute to enhancing the solution's gelation propensity.

2.4 Monitoring the critical assembly concentration (CAC) using thioflavin T assay

Thioflavin T (ThT) assay is a technique that is used to determine a minimum concentration, called the critical assembly concentration, at which the self-assembly of the samples to a more ordered fibrillar structure begins.[39] Thioflavin T was used as a fluorescent probe to measure the CAC value. It is a dye that gives an enhanced emission intensity at 480 nm upon binding to the fibrils and confirms the presence of β-sheets within the self-assembled structures.[2] The control samples of Fmoc-tyrosine-*t*Bu-OH, as seen in Fig. 8(a), show a gradual increase in the fluorescence intensity with increasing concentration, whereas the CAP-treated samples (5 and 10 minutes) showed an enhancement in the fluorescence intensity at a breakpoint of 10–50 μM (0.004–0.02 mg mL^{-1}), which corresponds to 0.0005–0.002 wt%.

For comparison, we followed the same protocol to determine the CAC value for Fmoc-tyrosine-OH samples; however, we did not observe any increase in the intensity of the CAP-treated samples. However, we found a minor enhancement in the 10-minute treated samples at around 500–1000 μM (0.2–0.4 mg mL^{-1}) concentration. Additionally, the untreated samples also exhibit a significant increase in ThT fluorescence, indicating the potential for fibril formation in the Fmoc-tyrosine-OH control samples in the medium (Fig. 8(b)). This also substantiates the earlier microscopy and rheological data, suggesting the presence of fibrils in the untreated Fmoc-tyrosine samples.

2.5 Mechanism for the CAP-induced self-assembled structures in the two peptide groups

Cold plasma produces a wide variety of potent reactive species that have been utilised in modulating the self-assembly of various aromatic amino acids, including L-tyrosine,[29,36,70,77] by inducing modulation in the reactive moieties of the amino acid. Thus, in this article, we investigated the effect of shielding L-tyrosine's reactive parts with protecting groups, primarily

Published on 29 ottobre 2025. Downloaded on 02/05/2026 06:27:29.

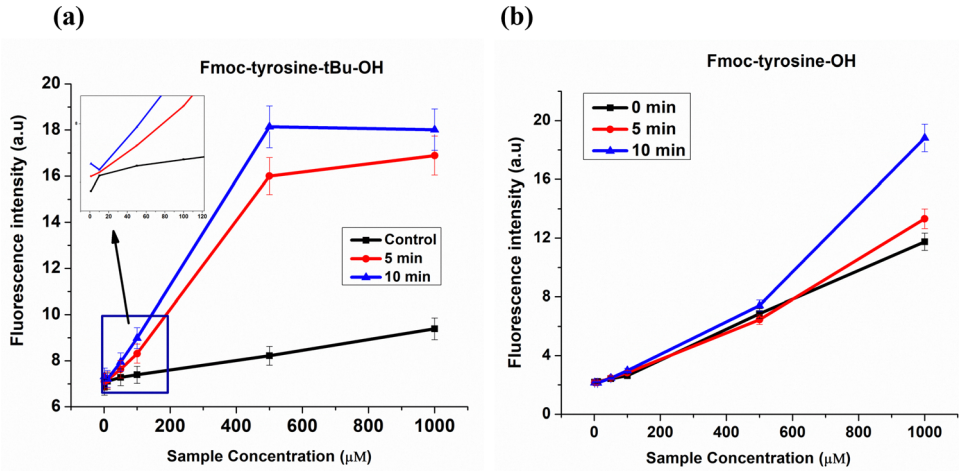

Fig. 8 Monitoring the CAC of Fmoc-Tyr(*t*Bu)-OH (a) and Fmoc-Tyr-OH (b) at different concentrations.

Fmoc and *tert*-butyl, and analysed the impact of CAP afterwards. The Fmoc group protects the amine functionality, while the *tert*-butyl group shields the phenolic moiety, limiting their direct interaction with CAP-generated reactive species. Interestingly, CAP-induced gelation was observed in Fmoc-Tyr(*t*Bu) samples, yielding fibrous supramolecular architectures even at 1 mM concentration. In contrast, Fmoc-Tyr did not produce a visible 3D network at the same concentration, though the initiation of gelation was observed at higher concentrations (>5 mM). This variation in the gelation behaviour of the two is consistent with the intrinsic hydrophobicity associated with the addition of the *t*Bu, which provides an additional steric hindrance, enhancing lipophilicity and favouring self-assembly in specific environments.[78,79] The aromaticity of the Fmoc unit, present in both the compounds, is known to promote hydrophobic and π–π stacking interactions of the fluorenyl rings.[39]

To understand the role of CAP-induced RONS in triggering the supramolecular assemblies, especially in promoting aggregation at a lower effective concentration, indicated by the CAC estimation, LC-MS/MS analysis was done. The findings reveal several modifications in the reactive part of the amino acid, particularly dominated by the oxidation and nitration of the aromatic rings present in Fmoc and L-tyrosine, which was also validated by the FTIR spectra.

The LCMS analysis further revealed possible oxidative/nitrative modifications in the CAP-treated samples, which occur due to the CAP's reactive species. These modifications affect both the physicochemical properties and the non-covalent interactions of the molecules, thereby altering their overall propensity to aggregate. The nitration, for example, introduces the strongly electron-withdrawing nitro group, which not only promotes the formation of β-sheet-rich aggregates,[80] but also alters its hydrophobicity, redox potential and steric bulkiness, all of which lead to impacting the noncovalent interactions among the molecules.[81] Similarly, oxidation of tyrosine to L-DOPA and quinones can alter the polarity and aromatic interactions of peptides.[82,83] Such chemical alterations accelerate the kinetics of aggregation, modify fibril morphology, and enhance the thermodynamic driving forces for assembly.

In addition to the physicochemical effects of nitration and hydroxylation on the amino acid, the hydrogen bonding of the reaction mixture is significantly enhanced by these modifications. An additional hydroxyl increases the number of hydrogen bond donor and acceptor sites. This enhances intermolecular hydrogen-bonding networks between the molecules. Similarly, the nitro group itself carries two oxygen atoms (electron-rich) that can act as hydrogen bond acceptors, allowing it to form an internal hydrogen bond with the phenolic hydroxyl group when both groups are appropriately oriented. Thus, nitrated tyrosine has extra H-bonding opportunities and promotes tighter intermolecular interactions. Fig. 9 shows the plausible mechanism by which the addition of these groups after CAP-induced modifications can lead to enhanced H-bonding in the system, along with the pre-existing π–π stacking in the Fmoc-tyrosine residue. The addition of *t*Bu to Fmoc-Tyr further increases the steric bulkiness of the sample, thereby augmenting the overall hydrophobicity and leading to visible supramolecular assemblies.

Overall, the chemical modifications induced by oxidation, nitration, or nitrosation modulate intermolecular non-covalent interactions by enhancing hydrogen bonding, as well as altering physicochemical properties, which is the key driving force behind increased aggregation and can lead to gel formation or fibrillation, as observed in our samples. The resulting supramolecular assemblies represent energetically stable configurations where the cumulative effect of enhanced hydrogen-bonding interactions drives the system toward its thermodynamic minimum, resulting in stable supramolecular architectures that persist under physiological conditions.

Thus, the incorporation of CAP and Fmoc-protection in an amino acid serves a dual purpose. Beyond shielding the amine group, the generated CAP-induced RONS interacted covalently or non-covalently with both the protecting groups and the parent amino acid, L-tyrosine. These interactions enhance the non-covalent interactions and overall hydrophobic–lipophilic balance of the molecules, thereby acting as a stimulus and providing the triggering force necessary for initiating the self-assembly process or phase transition required for supramolecular hydrogelation.

 This journal is © the Owner Societies 2025

Published on 29 ottobre 2025. Downloaded on 02/05/2026 06:27:29.

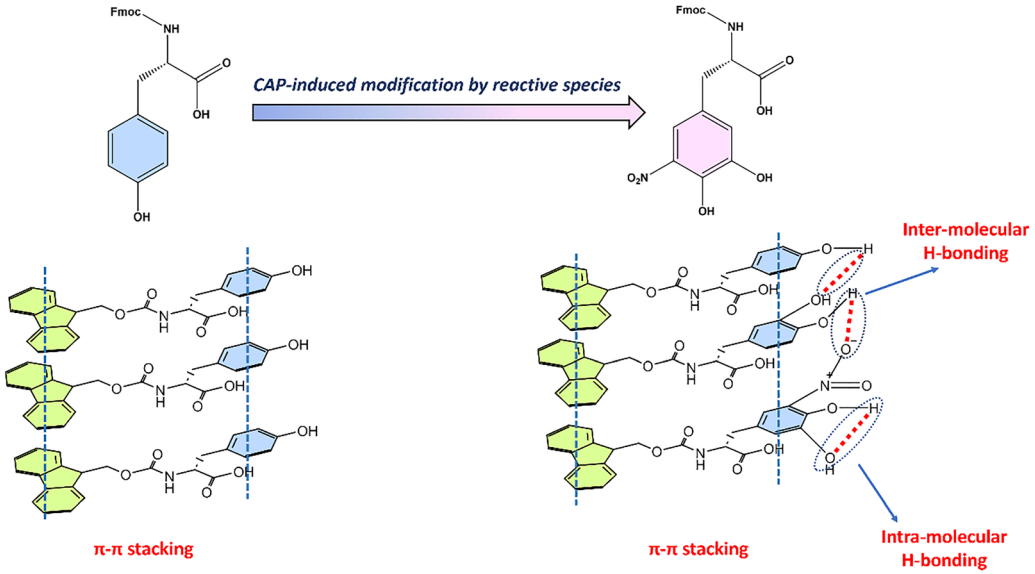

Fig. 9 Schematic showing the plausible mechanism of how CAP-induced chemical modifications in the phenolic ring of Fmoc-tyrosine increase hydrogen-bonding potential and promote supramolecular interactions.

3. Conclusion

In this article, we demonstrate the role of cold atmospheric plasma (CAP) in triggering the self-assembly of Fmoc-modified L-tyrosine amino acids, leading to the formation of microstructural architectures. The amino acids that underwent the CAP treatment self-assembled into unique 3-dimensional fibrous structures, with visible weak gelation in the Fmoc-Tyr(*t*Bu)-OH group, while forming complex mesh-like networks in the Fmoc-Tyr-OH group, as revealed by several microscopic images. The study introduced CAP as a novel strategy that can be an effective technique for designing functional soft materials, offering new insights into the fields of biomaterial fabrication and tissue engineering and other biomedical applications. The findings underlined the synergistic effect of CAP-induced RONS in enhancing the overall aromaticity and hydrophobicity of the environment by introducing multiple reactive species that alter the electronic conjugation of peptides, along with the hydrophilic–lipophilic balance of the molecules, subsequently facilitating the supramolecular aggregation. Unlike conventional methods that rely on pH modulation, solvent switching, or chemical additives, CAP presents a greener, cost-effective, and highly controllable approach for gelation. The reactive species generated by CAP initiate non-covalent interactions, facilitating molecular organization without additional crosslinkers or external stimuli. Thus, this study not only advances the fundamental understanding of CAP-driven self-assembly but also broadens its applicability toward functional material design.

4. Experimental section

4.1 Fmoc-modified amino acid solution preparation

Fmoc-L-tyrosine-OH and Fmoc-L-tyrosine-*t*Bu-OH were purchased from SRL, India. Fmoc-Cl was purchased from SRL, India. The Fmoc-protected amino acids were dissolved in a pH 7.4 phosphate buffer solution, with a concentration of 1 mM, prepared using ultrapure distilled water with a type-I resistivity of approximately 18.2 MΩ. All chemicals and reagents employed were utilised without the need for additional purification.

4.2 Cold atmospheric helium plasma jet system

The samples were treated using an indigenously developed single-jet CAP system (Fig. 10(a) and (b)), previously described in our publications, with its electrical characterization.[29,36] Briefly, the setup consists of a dielectric glass tube with a copper strip wrapped around (ground) and a stainless-steel rod (live) as electrodes that ionise the helium gas within a Teflon housing. The helium flow was maintained at 1.5 SLM using a variable flowmeter. Plasma parameters were maintained at a fixed 5 kV voltage and 25 kHz frequency throughout all experiments.

A 5 mL aliquot of the amino acid solution was poured into a glass Petri dish and positioned 5 mm beneath the plasma plume. During irradiation, primary reactive species from the plume interacted with atmospheric air to generate secondary reactive species, which subsequently reacted with the sample solution, initiating further reactions within it. All plasma parameters were maintained constant throughout the experiments, except for the treatment time, which was varied between 5 and 10 minutes. Following plasma exposure, the entire treated sample, including the formed soft fibrous architectures, was collected on vials using a pipette and used directly for bulk characterisation, unless otherwise specified.

4.3 Microscopic analysis (SEM, AFM, and TEM)

The samples were prepared by drop-casting 10 μL of solution on a clean glass slide and left for overnight drying. For the imaging of the supramolecular gels, the solutions containing the gels were carefully poured onto the glass slides using a micropipette and dried overnight. The samples were air-dried followed by

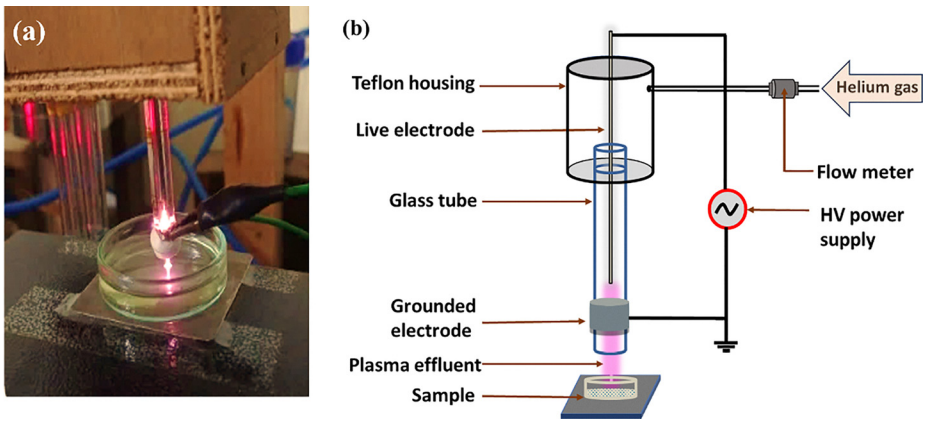

Fig. 10 A digital picture of an indigenously developed cold atmospheric plasma jet (a) and a schematic diagram of a CAP-jet (b).

Published on 29 ottobre 2025. Downloaded on 02/05/2026 06:27:29.

gold coating using a plasma sputtering technique. The model used for the SEM analysis was a Sigma-VP FESEM, Zeiss. A similar procedure was followed for AFM studies, which were done on freshly prepared drop-cast glass slides that were kept for overnight drying at room temperature. The experiments were performed using an AFM-NTEGRA, NTMDT in contact mode. For TEM analysis, the sample was diluted to 100 μM, and then a small drop was cast on the copper grid and left for vacuum drying overnight. The TEM analysis was done using a JEM-2100, JEOL.

4.4 Lyophilization of liquid samples

For removing the moisture content, 5 mL of non-treated and treated bulk solutions were kept at −80 °C overnight, before keeping the samples for freeze-drying in a lyophilizer (*Labonco*) to remove any excess moisture content. After 36 hours, the samples were fully dried and the samples were taken for powder analyses like pXRD, DSC, and FTIR.

4.5 XRD

Powder XRD was done on the lyophilised powder samples. The crystallinity was analysed using X-ray diffraction (XRD) apparatus (D8 Advance Bruker). A Cu Kα radiation source was operated at 40 kV with the 2θ range between 5° and 80°, 0.05° resolution and a scan rate of 0.5 min^{-1}. For analysing the crystallinity index and the crystallite size, OriginPro software was used. The raw patterns were baseline corrected, and peaks selected by the 'peak finder' in the software. The crystallinity % was calculated from the area of the crystalline peaks with respect to the total area in the range. The crystallite size was calculated using the Scherrer method

$$D(\mathrm{nm}) = \frac{K\lambda}{\beta \cos\theta}$$

where K is the Scherrer constant, which is taken as 0.9, λ is the wavelength of the X-ray radiation (0.15406), and β is the full width at half maximum (FWHM). The average crystallite sizes (D) are listed in Table 1 in the Results and discussion section.

4.6 Rheology

Rheological characterization was carried out in triplicate using a rotational MCR- Anton Paar rheometer. 100 μL of the sample, consisting of fibrous aggregates along with the liquid solution, was pipetted out and poured onto the base plate of the rheometer. This handling step may influence the microstructure of the sample, and therefore the rheological data presented reflect the viscoelastic properties of the transferred material rather than the *in situ* formed assembly. A conical plate (CP-50) geometry was used, and all measurements were performed at a constant temperature of 27 °C. The diameter of the plate was 50 mm, the cone angle was 1°, and the truncation was 103 μm. The measurement gap was kept at 0.1 mm for all the measurements.

4.7 DSC thermogram

The freeze-dried samples were taken for differential scanning calorimetric (DSC) analysis. The DSC studies were performed using a PerkinElmer instrument. The scanning was performed under a nitrogen atmosphere with a gas flow rate of 40 mL min^{-1}. First, the samples were held for 1.0 min at 25.00 °C and then heated from 25 °C to 440 °C at a heating rate of 20 °C min^{-1}.

4.8 UV-Visible spectroscopy

5 mL aliquots of the samples were subjected to CAP treatment under the conditions described above (treatment times: 5 and 10 min), after which 1 mL was immediately withdrawn for measurement. Before taking readings, the samples were diluted up to 50 μM with phosphate-buffered solution. The samples were analysed using a UV-1800-Shimadzu spectrophotometer, with 1 cm path length quartz cuvettes.

4.9 Steady-state fluorescence spectroscopy

Steady-state fluorescence studies were conducted using a Horiba spectrophotometer. The measurements were obtained using a 1-cm quartz cuvette with a 5 mm slit width. All samples (sol/gel) were excited at 265 nm, and emission data were collected at 290–500 nm.

 This journal is © the Owner Societies 2025

Published on 29 ottobre 2025. Downloaded on 02/05/2026 06:27:29.

4.10 FTIR

The samples were freeze-dried in a lyophilizer (*Labonco*) to remove any excess moisture content before being analysed for FTIR. FTIR was run on the PerkinElmer spectrometer in the 400 to 4000 cm^{-1} range, with a scan resolution of 40 cm^{-1}.

4.11 CD

For CD analysis, the solutions were equilibrated using a pipette and were diluted up to 250 μM, following which 200 μL aliquots of the native and CAP-treated amino acid solution were put on a Quartz cell of path length 0.1 cm and analysed on a Jasco J-1500 spectrophotometer.

4.12 Zeta potential analysis

The zeta potential of the treated and untreated samples was measured using the zeta sizer (Malvern Analytical-NanoZS90). The measurements were repeated in triplicate, and the average values were plotted and reported.

4.13 Liquid chromatography-tandem mass spectroscopy (LC MS/MS)

Mass spectra were acquired on a Thermo Scientific Q Exactive Plus quadrupole–Orbitrap hybrid mass spectrometer (Thermo Fisher Scientific) equipped with an electrospray ionization (ESI) source. A Dionex Ultimate 3000 (Thermo) HPLC equipped with an RP C-18 analytical (XSelect HSS T3, 3.5 μm, 3 × 150 mm) HPLC column was used. Gradient grade HPLC solvents from Merck were used as the mobile phases. Silica gel (Merck, 100–200 mesh size) and SUPELCO Diaion HP-20 from Sigma Aldrich were used for column chromatography. The MS studies were conducted in positive and negative modes *via* electrospray ionization with a mass-to-charge ratio (m/z) range of 200 to 1200, an automatic gain control (AGC) target of 3×10^6, and a resolution of 140 000. For data recording in both positive and negative modes, scan rates of 1.0 scans per second were employed. The mobile phase consisted of an isocratic gradient of acetonitrile/water 50 : 50 (v/v) and was applied for 30 min with a flow rate of 0.4 mL min^{-1}. Raw data were processed using an Xcalibur (Thermo Fisher Scientific).

4.14 CGC

1 mM stock solution was diluted at varying concentrations (1 μM, 10 μM, 50 μM, 100 μM and 500 μM) in PBS (pH 7.4), and treated with CAP (5- and 10-minutes). After that, 50 μM ThT solution was added to the samples (untreated and treated) in a 1 : 1 ratio, incubated for 30 min, and fluorescence was measured in a GM-3000 Promega multimode reader with excitation at 475 nm and emission at 495–500 nm. The measurement was taken in triplicate, plotted, and checked for the increase in the fluorescence intensity.

Conflicts of interest

The authors declare no conflicts of interest.

Data availability

Supplementary information (SI): Fig S1: 2D chemical structure of Fmoc-L-tyrosine and Fmoc-Tyr(*t*Bu)-OH. Fig S2: AFM images of Fmoc-Tyr(*t*Bu)-OH. Fig S3: Pictures of assemblies created by Fmoc-Tyr-OH at higher concentration. Fig S4: Loss factor with respect to angular frequency, showing the independence of loss factor with angular frequency, a criterion indicating the formation of gels. Fig S5: Crossover frequencies decreasing with increasing CAP treatment time in the case of Fmoc-Tyr(*t*Bu)-OH. Fig S6: DSC thermogram of the (a) Fmoc-tyrosine (b) Fmoc-Tyr(*t*Bu)-OH. Fig S7: Blue shifting of the UV-Vis absorbance peak (a) Fmoc-Tyr(*t*Bu)-OH (b) Fmoc tyrosine. Fig S8 and S9: Effect of individual species (H_2O_2 and NO_3^-) on the samples Table S1: Area under the curve of the DSC thermogram. See DOI: https://doi.org/10.1039/d5cp02585k.

The data supporting this article have been included as part of the supplementary information.

Acknowledgements

The author KS thanks the ICMR Project grant (File No. 17x(3)/Ad-hoc/19/2022-ITR dt. 23.12.2022) and the DST-IASST, Guwahati in-house project grant. The author PB thanks IASST, DST, Govt. of India for supporting the Junior Research Fellowship and AcSIR for PhD registration. The authors thank SAIC-IASST for the instrumentation facilities.

References

1 X. Du, J. Zhou, J. Shi and B. Xu, Supramolecular Hydrogelators and Hydrogels: From Soft Matter to Molecular Biomaterials, *Chem. Rev.*, 2015, **115**(24), 13165–13307, DOI: 10.1021/acs.chemrev.5b00299.

2 P. Zhou, R. Xing, Q. Li, J. Li, C. Yuan and X. Yan, Steering Phase-Separated Droplets to Control Fibrillar Network Evolution of Supramolecular Peptide Hydrogels, *Matter*, 2023, **6**(6), 1945–1963, DOI: 10.1016/j.matt.2023.03.029.

3 D. T. Seroski and G. A. Hudalla, Self-Assembled Peptide and Protein Nanofibers for Biomedical Applications, *Biomed. Appl. Funct. Nanomater.*, 2018, 569–598, DOI: 10.1016/B978-0-323-50878-0.00019-7.

4 R. Khan, E. Ahmad, M. Zaman, A. Qadeer and G. Rabbani, Nanoparticles in Relation to Peptide and Protein Aggregation, *Int. J. Nanomed.*, 2014, 899, DOI: 10.2147/IJN.S54171.

5 P. Singh, S. K. Brar, M. Bajaj, N. Narang, V. S. Mithu, O. P. Katare, N. Wangoo and R. K. Sharma, Self-Assembly of Aromatic α-Amino Acids into Amyloid Inspired Nano/Micro Scaled Architects, *Mater. Sci. Eng., C*, 2017, **72**, 590–600, DOI: 10.1016/j.msec.2016.11.117.

6 C. Ménard-Moyon, V. Venkatesh, K. V. Krishna, F. Bonachera, S. Verma and A. Bianco, Self-Assembly of Tyrosine into Controlled Supramolecular Nanostructures, *Chem. – Eur. J.*, 2015, **21**(33), 11681–11686, DOI: 10.1002/chem.201502076.

7 F. Prencipe, C. Diaferia, F. Rossi, L. Ronga and D. Tesauro, Forward Precision Medicine: Micelles for Active Targeting

Published on 29 ottobre 2025. Downloaded on 02/05/2026 06:27:29.

Driven by Peptides, *Molecules*, 2021, **26**(13), 4049, DOI: 10.3390/molecules26134049.
8 C. Dai, Y. Zhang, M. Gao, Y. Li, W. Lv, X. Wang, Y. Wu and M. Zhao, The Study of a Novel Nanoparticle-Enhanced Wormlike Micellar System, *Nanoscale Res. Lett.*, 2017, **12**(1), 431, DOI: 10.1186/s11671-017-2198-2.
9 G. Yang, H. Ding, Z. Kochovski, R. Hu, Y. Lu, Y. Ma, G. Chen and M. Jiang, Highly Ordered Self-Assembly of Native Proteins into 1D, 2D, and 3D Structures Modulated by the Tether Length of Assembly-Inducing Ligands, *Angew. Chem., Int. Ed.*, 2017, **56**(36), 10691–10695, DOI: 10.1002/anie.201703052.
10 L. E. R. O'Leary, J. A. Fallas, E. L. Bakota, M. K. Kang and J. D. Hartgerink, Multi-Hierarchical Self-Assembly of a Collagen Mimetic Peptide from Triple Helix to Nanofibre and Hydrogel, *Nat. Chem.*, 2011, **3**(10), 821–828, DOI: 10.1038/nchem.1123.
11 J. M. Alonso, J. Andrade del Olmo, R. Perez Gonzalez and V. Saez-Martinez, Injectable Hydrogels: From Laboratory to Industrialization, *Polymers*, 2021, **13**(4), 650, DOI: 10.3390/polym13040650.
12 S. Strandman and X. X. Zhu, Self-Healing Supramolecular Hydrogels Based on Reversible Physical Interactions, *Gels*, 2016, **2**(2), 16, DOI: 10.3390/gels2020016.
13 S. Wang, Z. Wang, S. E. M. Foo, N. S. Tan, Y. Yuan, W. Lin, Z. Zhang and K. W. Ng, Culturing Fibroblasts in 3D Human Hair Keratin Hydrogels, *ACS Appl. Mater. Interfaces*, 2015, **7**(9), 5187–5198, DOI: 10.1021/acsami.5b00854.
14 M. Živanić, A. Espona-Noguera, H. Verswyvel, E. Smits, A. Bogaerts, A. Lin and C. Canal, Injectable Plasma-Treated Alginate Hydrogel for Oxidative Stress Delivery to Induce Immunogenic Cell Death in Osteosarcoma, *Adv. Funct. Mater.*, 2024, **34**(14), 2312005, DOI: 10.1002/adfm.202312005.
15 Y. Zhang, J. Zhang, J. Li, E. Gazit and K. Tao, Minimalistic Peptide Assemblies for Sustainable Optoelectronics, *Peptide Self-Assembly and Engineering*, Wiley, 2024, pp. 241–261, DOI: 10.1002/9783527841264.ch11.
16 A. Lakshmanan, S. Zhang and C. A. E. Hauser, Short Self-Assembling Peptides as Building Blocks for Modern Nanodevices, *Trends Biotechnol.*, 2012, **30**(3), 155–165, DOI: 10.1016/j.tibtech.2011.11.001.
17 K. Barriales, S. Khandaker, A. Jain, D. Sementa, M. N. Nair, T. Wang, J. Tang, C. DelRe and R. V. Ulijn, Aqueous Graphene Dispersion and Biofunctionalization via Enzymatic Oxidation of Tripeptides, *Small*, 2024, **20**(38), 2400775, DOI: 10.1002/smll.202400775.
18 I. W. Hamley, Self-Assembly, Bioactivity, and Nanomaterials Applications of Peptide Conjugates with Bulky Aromatic Terminal Groups, *ACS Appl. Bio Mater.*, 2023, **6**(2), 384–409, DOI: 10.1021/acsabm.2c01041.
19 A. Mahler, M. Reches, M. Rechter, S. Cohen and E. Gazit, Rigid, Self-Assembled Hydrogel Composed of a Modified Aromatic Dipeptide, *Adv. Mater.*, 2006, **18**(11), 1365–1370, DOI: 10.1002/adma.200501765.
20 B. Das Gupta, A. Halder, T. Vijayakanth, N. Ghosh, R. Konar, O. Mukherjee, E. Gazit and S. Mondal, A Broad-Spectrum Antibacterial Hydrogel Based on the Synergistic Action of Fmoc–Phenylalanine and Fmoc–Lysine in a Co-Assembled State, *J. Mater. Chem. B*, 2024, **12**(34), 8444–8453, DOI: 10.1039/D4TB00948G.
21 N. Balasco, D. Altamura, P. L. Scognamiglio, T. Sibillano, C. Giannini, G. Morelli, L. Vitagliano, A. Accardo and C. Diaferia, Self-Assembled Materials Based on Fully Aromatic Peptides: The Impact of Tryptophan, Tyrosine, and Dopa Residues, *Langmuir*, 2024, **40**(2), 1470–1486, DOI: 10.1021/acs.langmuir.3c03214.
22 A. Chandran, K. R. Athulya, T. R. Bantu and A. C. Kumar, Fluorescence Studies of Amino Acid and Peptide-Based Hydrogels: Unveiling Self-Assembly and Structural Insights, *ChemistrySelect*, 2025, **10**(8), e202405721, DOI: 10.1002/slct.202405721.
23 V. Castelletto, L. de Mello, E. R. da Silva, J. Seitsonen and I. W. Hamley, Comparison of the Self-assembly and Cytocompatibility of Conjugates of Fmoc (9-fluorenylmethoxycarbonyl) with Hydrophobic, Aromatic, or Charged Amino Acids, *J. Pept. Sci.*, 2024, **30**(6), e3571, DOI: 10.1002/psc.3571.
24 X. Du, J. Zhou, J. Shi and B. Xu, Supramolecular Hydrogelators and Hydrogels: From Soft Matter to Molecular Biomaterials, *Chem. Rev.*, 2015, **115**(24), 13165–13307, DOI: 10.1021/acs.chemrev.5b00299.
25 G. Pulat, E. Bilgiç, U. K. Ercan and O. Karaman, Enhanced Osteogenic Differentiation via Collagen and BMP-2 Mimetic Peptide Conjugation to β-TCP Scaffolds Using a Cold Atmospheric Plasma-Assisted Strategy, *ACS Appl. Bio Mater.*, 2025, **8**(3), 2569–2579, DOI: 10.1021/acsabm.5c00029.
26 S. Roux, A. Marchès, S. Galiacy, N. Merbahi and M. Simon, Biological Solutions Activated by Cold Plasma at Atmospheric Pressure: A New Therapeutic Approach for Skin Wound Healing, *Biomed. Pharmacother.*, 2025, **186**, 118001, DOI: 10.1016/j.biopha.2025.118001.
27 I. Plattfaut, M. Besser, A.-L. Severing, E. K. Stürmer and C. Opländer, Plasma Medicine and Wound Management: Evaluation of the Antibacterial Efficacy of a Medically Certified Cold Atmospheric Argon Plasma Jet, *Int. J. Antimicrob. Agents*, 2021, **57**(5), 106319, DOI: 10.1016/j.ijantimicag.2021.106319.
28 N. Zhang, G. Yang, Y. Wu, L. Hu, C. Zhao, H.-H. Liu, L. Wu, J. Pan and X. Liu, Controlled Release of Cold Atmospheric Plasma by Gelatin Scaffold Enhances Wound Healing via Macrophage Modulation, *ACS Appl. Mater. Interfaces*, 2025, **17**(10), 15050–15066, DOI: 10.1021/acsami.4c21635.
29 P. Bhatt and K. Sankaranarayanan, Insights Into Cold Atmospheric Plasma Triggered Self-Assembly of Keratin Protein, *Plasma Processes Polym.*, 2025, **22**(6), 70003, DOI: 10.1002/ppap.70003.
30 A. Lavrikova, M. Janda, H. Bujdáková and K. Hensel, Eradication of Single- and Mixed-Species Biofilms of P. Aeruginosa and S. Aureus by Pulsed Streamer Corona Discharge Cold Atmospheric Plasma, *Sci. Total Environ.*, 2025, **959**, 178184, DOI: 10.1016/j.scitotenv.2024.178184.
31 V. S. Mbanugo, B. S. Ojo, T. C. Lin, Y.-W. Huang, M. Locmelis and D. Han, Per- and Polyfluoroalkyl Substance (PFAS) Degradation in Water and Soil Using Cold Atmospheric Plasma (CAP): A Review, *ACS Phys. Chem. Au*, 2025, **5**(2), 117–133, DOI: 10.1021/acsphyschemau.4c00092.

 This journal is © the Owner Societies 2025

Published on 29 ottobre 2025. Downloaded on 02/05/2026 06:27:29.

32 M. M. Nasiru, E. F. Boateng, F. Alnadari, H. K. Bako, H. I. Ibeogu, J. Feng, J. Song, H. Liu, Q. Zhang, K. Masisi, C. M. Roth, W. Yan, J. Zhang and C. Li, Cold Plasma Reengineers Peanut Protein Isolate: Unveiling Changes in Functionality, Rheology, and Structure, *Int. J. Biol. Macromol.*, 2025, **286**, 138407, DOI: **10.1016/j.ijbiomac.2024.138407**.

33 P. P. Akhila, K. V. Sunooj, M. R. Nemţanu, T. Sakshi, B. Aaliya, M. Navaf, A. Annamalai, B. Indumathy, S. Yugeswaran, S. K. Sinha, D. N. Yadav, M. C. Joshi, A. Jebreen, K. P. Sudheer and J. George, 3D Printing of Hausa Potato Starch: Assessing a New Dimension of Cold Plasma Treatment Using Varied Feed Gas, *Int. J. Biol. Macromol.*, 2025, **302**, 140655, DOI: **10.1016/j.ijbiomac.2025.140655**.

34 S. Sharma, H. Prabhakar and R. K. Singh, Atmospheric Cold Plasma-Induced Changes in Milk Proteins, *Food Bioprocess Technol.*, 2022, **15**(12), 2737–2748, DOI: **10.1007/s11947-022-02915-z**.

35 B. Bhattacharjee, R. Bezbaruah, D. Rynjah, A. Newar, S. Sengupta, P. Pegu, N. Dey, S. Bora and D. Barman, Cold Atmospheric Plasma: A Noteworthy Approach in Medical Science, *Sci. Pharm.*, 2023, **2**(2), 46–76, DOI: **10.58920/sciphar02020046**.

36 P. Bhatt, P. S. Garad, V. V. S. P. K. Rayala, P. Radhakrishnanand and K. Sankaranarayanan, Non-Thermal Plasma Modulated L-Tyrosine Self-Assemblies: A Potential Avenue for Fabrication of Supramolecular Self-Assembled Biomaterials, *RSC Adv.*, 2024, **14**(20), 13984–13996, DOI: **10.1039/D4RA01891E**.

37 P. Singh, S. Misra, A. Das, S. Roy, P. Datta, G. Bhattacharjee, B. Satpati and J. Nanda, Supramolecular Hydrogel from an Oxidized Byproduct of Tyrosine, *ACS Appl. Bio Mater.*, 2019, **2**(11), 4881–4891, DOI: **10.1021/acsabm.9b00637**.

38 E. R. Draper, K. L. Morris, M. A. Little, J. Raeburn, C. Colquhoun, E. R. Cross, T. O. McDonald, L. C. Serpell and D. J. Adams, Hydrogels Formed from Fmoc Amino Acids, *CrystEngComm*, 2015, **17**(42), 8047–8057, DOI: **10.1039/C5CE00801H**.

39 T. Wang, C. Ménard-Moyon and A. Bianco, Structural Transformation of Coassembled Fmoc-Protected Aromatic Amino Acids to Nanoparticles, *ACS Appl. Mater. Interfaces*, 2024, **16**(8), 10532–10544, DOI: **10.1021/acsami.3c18463**.

40 N. Balasco, D. Altamura, P. L. Scognamiglio, T. Sibillano, C. Giannini, G. Morelli, L. Vitagliano, A. Accardo and C. Diaferia, Self-Assembled Materials Based on Fully Aromatic Peptides: The Impact of Tryptophan, Tyrosine, and Dopa Residues, *Langmuir*, 2024, **40**(2), 1470–1486, DOI: **10.1021/acs.langmuir.3c03214**.

41 K. Thornton, Y. M. Abul-Haija, N. Hodson and R. V. Ulijn, Mechanistic Insights into Phosphatase Triggered Self-Assembly Including Enhancement of Biocatalytic Conversion Rate, *Soft Matter*, 2013, **9**(39), 9430, DOI: **10.1039/c3sm51177d**.

42 N. Gour, V. Kshtriya, B. Koshti, H. Narode and S. Naskar Controlled Self-Assembly of Modified Aromatic Amino Acids. 2021, DOI: **10.26434/chemrxiv-2021-p7d0s-v2**.

43 C. Guilbaud-Chéreau, B. Dinesh, R. Schurhammer, D. Collin, A. Bianco and C. Ménard-Moyon, Protected Amino Acid–Based Hydrogels Incorporating Carbon Nanomaterials for Near-Infrared Irradiation-Triggered Drug Release, *ACS Appl. Mater. Interfaces*, 2019, **11**(14), 13147–13157, DOI: **10.1021/acsami.9b02482**.

44 P. Zhang, Y. Huang, Y. T. Kwon and S. Li, PEGylated Fmoc–Amino Acid Conjugates as Effective Nanocarriers for Improved Drug Delivery, *Mol. Pharmaceutics*, 2015, **12**(5), 1680–1690, DOI: **10.1021/acs.molpharmaceut.5b00157**.

45 G. Aykent, C. Zeytun, A. Marion and S. Özçubukçu, Simple Tyrosine Derivatives Act as Low Molecular Weight Organogelators, *Sci. Rep.*, 2019, **9**(1), 4893, DOI: **10.1038/s41598-019-41142-z**.

46 M. A. Oliver, L. K. Hussein, E. A. Molina, J. W. Keyloun, S. M. McKnight, L. M. Jimenez, L. T. Moffatt, J. W. Shupp and B. C. Carney, Cold Atmospheric Plasma Is Bactericidal to Wound-Relevant Pathogens and Is Compatible with Burn Wound Healing, *Burns*, 2024, **50**(5), 1192–1212, DOI: **10.1016/j.burns.2023.12.012**.

47 G. Isbary, G. Morfill, H. U. Schmidt, M. Georgi, K. Ramrath, J. Heinlin, S. Karrer, M. Landthaler, T. Shimizu, B. Steffes, W. Bunk, R. Monetti, J. L. Zimmermann, R. Pompl and W. Stolz, A First Prospective Randomized Controlled Trial to Decrease Bacterial Load Using Cold Atmospheric Argon Plasma on Chronic Wounds in Patients, *Br. J. Dermatol.*, 2010, **163**(1), 78–82, DOI: **10.1111/j.1365-2133.2010.09744.x**.

48 T. Maho, R. Binois, F. Brulé-Morabito, M. Demasure, C. Douat, S. Dozias, P. Escot Bocanegra, I. Goard, L. Hocqueloux, C. Le Helloco, I. Orel, J.-M. Pouvesle, T. Prazuck, A. Stancampiano, C. Tocaben and E. Robert, Anti-Bacterial Action of Plasma Multi-Jets in the Context of Chronic Wound Healing, *Appl. Sci.*, 2021, **11**(20), 9598, DOI: **10.3390/app11209598**.

49 J. Douglas, Weak and Strong Gels and the Emergence of the Amorphous Solid State, *Gels*, 2018, **4**(1), 19, DOI: **10.3390/gels4010019**.

50 A. Karoyo and L. Wilson, Physicochemical Properties and the Gelation Process of Supramolecular Hydrogels: A Review, *Gels*, 2017, **3**(1), 1, DOI: **10.3390/gels3010001**.

51 S. Bianco, S. Panja and D. J. Adams, Using Rheology to Understand Transient and Dynamic Gels, *Gels*, 2022, **8**(2), 132, DOI: **10.3390/gels8020132**.

52 A. Croitoriu, L. E. Nita, A. P. Chiriac, A. G. Rusu and M. Bercea, New Physical Hydrogels Based on Co-Assembling of FMOC–Amino Acids, *Gels*, 2021, **7**(4), 208, DOI: **10.3390/gels7040208**.

53 G. Stojkov, Z. Niyazov, F. Picchioni and R. K. Bose, Relationship between Structure and Rheology of Hydrogels for Various Applications, *Gels*, 2021, **7**(4), 255, DOI: **10.3390/gels7040255**.

54 P. Santos, M. Carignano and O. Campanella, Effect of Shear History on Rheology of Time-Dependent Colloidal Silica Gels, *Gels*, 2017, **3**(4), 45, DOI: **10.3390/gels3040045**.

55 D. Germain and M.-A. Ouellet, Subaerial Sediment-Water Flows on Hillslopes, *Prog. Phys. Geogr.: Earth Environ.*, 2013, **37**(6), 813–833, DOI: **10.1177/0309133313507943**.

56 Y. Tang, M. Hu, F. Tang, R. Huang, H. Wang, D. Wu and P. Lan, Easily-Injectable Shear-Thinning Hydrogel Provides Long-Lasting Submucosal Barrier for Gastrointestinal Endoscopic Surgery, *Bioact. Mater.*, 2022, **15**, 44–52, DOI: **10.1016/j.bioactmat.2021.11.026**.

Published on 29 ottobre 2025. Downloaded on 02/05/2026 06:27:29.

57 Y. Gokarn, S. Agarwal, K. Arthur, A. Bepperling, E. S. Day, D. Filoti, D. G. Greene, D. Hayes, R. Kroe-Barrett, T. Laue, J. Lin, B. McGarry, V. Razinkov, S. Singh, R. Taing, S. Venkataramani, W. Weiss, D. Yang and I. E. Zarraga *Biophysical Techniques for Characterizing the Higher Order Structure and Interactions of Monoclonal Antibodies*, 2015, pp. 285–327, DOI: **10.1021/bk-2015-1201.ch006**.

58 K. Bowers and N. Markova *Value of DSC in Characterization and Optimization of Protein Stability*, 2019, pp. 33–44, DOI: **10.1007/978-1-4939-9179-2_3**.

59 P. G. Argudo, R. Contreras-Montoya, L. Álvarez de Cienfuegos, J. M. Cuerva, M. Cano, D. Alba-Molina, M. T. Martín-Romero, L. Camacho and J. J. Giner-Casares, Unravelling the 2D Self-Assembly of Fmoc-Dipeptides at Fluid Interfaces, *Soft Matter*, 2018, **14**(46), 9343–9350, DOI: **10.1039/C8SM01508B**.

60 Y. Zou, K. Razmkhah, N. P. Chmel, I. W. Hamley and A. Rodger, Spectroscopic Signatures of an Fmoc–Tetrapeptide, Fmoc and Fluorene, *RSC Adv.*, 2013, **3**(27), 10854, DOI: **10.1039/c3ra41979g**.

61 Y. Deng, W. Yuan, Z. Jia and G. Liu, H- and J-Aggregation of Fluorene-Based Chromophores, *J. Phys. Chem. B*, 2014, **118**(49), 14536–14545, DOI: **10.1021/jp510520m**.

62 Z. Yan, H. Xu, S. Guang, X. Zhao, W. Fan and X. Y. Liu, A Convenient Organic–Inorganic Hybrid Approach Toward Highly Stable Squaraine Dyes with Reduced H-Aggregation, *Adv. Funct. Mater.*, 2012, **22**(2), 345–352, DOI: **10.1002/adfm.201101565**.

63 R. Orbach, L. Adler-Abramovich, S. Zigerson, I. Mironi-Harpaz, D. Seliktar and E. Gazit, Self-Assembled Fmoc-Peptides as a Platform for the Formation of Nanostructures and Hydrogels, *Biomacromolecules*, 2009, **10**(9), 2646–2651, DOI: **10.1021/bm900584m**.

64 P. Chakraborty, Y. Tang, T. Yamamoto, Y. Yao, T. Guterman, S. Zilberzwige-Tal, N. Adadi, W. Ji, T. Dvir, A. Ramamoorthy, G. Wei and E. Gazit, Unusual Two-Step Assembly of a Minimalistic Dipeptide-Based Functional Hypergelator, *Adv. Mater.*, 2020, **32**(9), 1906043, DOI: **10.1002/adma.201906043**.

65 K. B. Davis, Z. Zhang, E. A. Karpova and J. Zhang, Application of Tyrosine-Tryptophan Fluorescence Resonance Energy Transfer in Monitoring Protein Size Changes, *Anal. Biochem.*, 2018, **557**, 142–150, DOI: **10.1016/j.ab.2018.07.022**.

66 L. Yang, X. Wang, G. Zhang, X. Chen, G. Zhang and J. Jiang, Aggregation-Induced Intersystem Crossing: A Novel Strategy for Efficient Molecular Phosphorescence, *Nanoscale*, 2016, **8**(40), 17422–17426, DOI: **10.1039/C6NR03656B**.

67 P. Bhatt, Reema and K. Sankaranarayanan, Cold Atmospheric Plasma as a Promising Medical Device for Wound Healing: Implications from Protein Perspective, *Regener. Eng. Transl. Med.*, 2025, DOI: **10.1007/s40883-025-00410-3**.

68 S. Fleming, P. W. J. M. Frederix, I. Ramos Sasselli, N. T. Hunt, R. V. Ulijn and T. Tuttle, Assessing the Utility of Infrared Spectroscopy as a Structural Diagnostic Tool for β-Sheets in Self-Assembling Aromatic Peptide Amphiphiles, *Langmuir*, 2013, **29**(30), 9510–9515, DOI: **10.1021/la400994v**.

69 A. M. Smith, R. J. Williams, C. Tang, P. Coppo, R. F. Collins, M. L. Turner, A. Saiani and R. V. Ulijn, Fmoc-Diphenylalanine Self Assembles to a Hydrogel via a Novel Architecture Based on π–π Interlocked B-Sheets, *Adv. Mater.*, 2008, **20**(1), 37–41, DOI: **10.1002/adma.200701221**.

70 E. Takai, T. Kitamura, J. Kuwabara, S. Ikawa, S. Yoshizawa, K. Shiraki, H. Kawasaki, R. Arakawa and K. Kitano, Chemical Modification of Amino Acids by Atmospheric-Pressure Cold Plasma in Aqueous Solution, *J. Phys. D: Appl. Phys.*, 2014, **47**(28), 285403, DOI: **10.1088/0022-3727/47/28/285403**.

71 S. Arndt, F. Fadil, K. Dettmer, P. Unger, M. Boskovic, C. Samol, A.-K. Bosserhoff, J. L. Zimmermann, M. Gruber, W. Gronwald and S. Karrer, Cold Atmospheric Plasma Changes the Amino Acid Composition of Solutions and Influences the Anti-Tumor Effect on Melanoma Cells, *Int. J. Mol. Sci.*, 2021, **22**(15), 7886, DOI: **10.3390/ijms22157886**.

72 V. A. Adhav and K. Saikrishnan, The Realm of Unconventional Noncovalent Interactions in Proteins: Their Significance in Structure and Function, *ACS Omega*, 2023, **8**(25), 22268–22284, DOI: **10.1021/acsomega.3c00205**.

73 S. Bartesaghi and R. Radi, Fundamentals on the Biochemistry of Peroxynitrite and Protein Tyrosine Nitration, *Redox Biol.*, 2018, **14**, 618–625, DOI: **10.1016/j.redox.2017.09.009**.

74 R. Radi, Nitric Oxide, Oxidants, and Protein Tyrosine Nitration, *Proc. Natl. Acad. Sci. U. S. A.*, 2004, **101**(12), 4003–4008, DOI: **10.1073/pnas.0307446101**.

75 R. R. Khanikar, M. Kalita, P. Kalita, B. Kashyap, S. Das, M. R. Khan, H. Bailung and K. Sankaranarayanan, Cold Atmospheric Pressure Plasma for Attenuation of SARS-CoV-2 Spike Protein Binding to ACE2 Protein and the RNA Deactivation, *RSC Adv.*, 2022, **12**(15), 9466–9472, DOI: **10.1039/D2RA00009A**.

76 N. Puač and N. Škoro, Plasma–Liquid Interaction for Agriculture—A Focused Review, *Plasma Processes Polym.*, 2025, **22**(1), 2400208, DOI: **10.1002/ppap.202400208**.

77 K.-C. Hsieh and Y. Ting, Atmospheric Cold Plasma Reduces Ara h 1 Antigenicity in Roasted Peanuts by Altering the Protein Structure and Amino Acid Profile, *Food Chem.*, 2024, **441**, 138115, DOI: **10.1016/j.foodchem.2023.138115**.

78 Q. A. K. Nisa, D. H. Son, R. F. B. Nasrun and J. H. Kim, Understanding Charge Recombination and Light-Induced Degradation: An in-Depth Study of *Tert*-Butyl Modified Carbazole-Based Self-Assembled Monolayers for Enhanced Performance in Organic Solar Cells, *J. Mater. Chem. A*, 2025, **13**, 10967–10979, DOI: **10.1039/D4TA09141H**.

79 O. J. Donadel, T. Martín, V. S. Martín, J. Villar and J. M. Padrón, The *tert*-Butyl Dimethyl Silyl Group as an Enhancer of Drug Cytotoxicity against Human Tumor Cells, *Bioorg. Med. Chem. Lett.*, 2005, **15**(15), 3536–3539, DOI: **10.1016/j.bmcl.2005.05.126**.

80 A. A. Profit, V. Felsen, J. Chinwong, E. E. Mojica and R. Z. B. Desamero, Evidence of Π-stacking Interactions in the Self-assembly of HIAPP 22-29, *Proteins: Struct., Funct., Bioinf.*, 2013, **81**(4), 690–703, DOI: **10.1002/prot.24229**.

81 T. Long, L. Liu, Y. Tao, W. Zhang, J. Quan, J. Zheng, J. D. Hegemann, M. Uesugi, W. Yao, H. Tian and H. Wang, Light-

 This journal is © the Owner Societies 2025

Controlled Tyrosine Nitration of Proteins, *Angew. Chem., Int. Ed.*, 2021, **60**(24), 13414–13422, DOI: **10.1002/anie.202102287**.

82 A. Ganesan, N. Mohammadi and F. Wang, From Building Blocks of Proteins to Drugs: A Quantum Chemical Study on Structure–Property Relationships of Phenylalanine, Tyrosine and Dopa, *RSC Adv.*, 2014, **4**(17), 8617, DOI: **10.1039/c3ra47364c**.

83 M. B. Feeney and C. Schöneich, Tyrosine Modifications in Aging, *Antioxid. Redox Signaling*, 2012, **17**(11), 1571–1579, DOI: **10.1089/ars.2012.4595**.

Published on 29 ottobre 2025. Downloaded on 02/05/2026 06:27:29.